SANS/USANS Study of the New Albany Shale: A Treatise on Microporosity

Jitendra Bahadur[1], Andrzej Radlinski[2], Yuri B. Melnichenko[1*], Maria Mastalerz[3], Arndt Schimmelmann[4]

[1]Biology and Soft Matter Division, Oak Ridge National Laboratory, Oak Ridge, TN 37831-6393, USA

[2]Queensland Micro and Nanotechnology Centre, Griffith University, Nathan 4111, Brisbane, Australia

[3]Indiana Geological Survey, [4]Department of Geological Sciences, Indiana University, Bloomington, IN 47405-2208, USA

Abstract

Small-angle neutron scattering (SANS) and ultra small-angle neutron scattering (USANS) techniques were applied to study the microstructure of several New Albany shales of different maturity. It has been established that total porosity decreases with maturity and somewhat increases for post-mature samples. A new method of SANS data analysis was developed, which allows extracting information about the size range and number density of micropores from the relatively flat scattering intensity observed in the limit of large scattering vector Q. Macropores and significant number of mesopores are surface fractals and their structure can be described in terms of the polydisperse spheres (PDSP) model. The model independent Porod invariant method was employed to estimate total porosity and the results were compared with the PDSP model results. It has been demonstrated that independent evaluation of incoherent background is crucial for accurate interpretation of the scattering data in the limit of large Q-values. Pore volumes

estimated by the N_2 and CO_2 adsorption as well as mercury adsorption technique have been compared with those measured by SANS/USANS, and possible reasons for the observed discrepancies are discussed.

Keywords: New Albany Shale, Maturity, SANS, USANS, Porosity, Gas Adsorption

*Corresponding author: Tel: +1 865 576 7746, *Email:* melnichenkoy@ornl.gov

1. Introduction

Porosity is the key structural factor that defines the ability of shale to store natural gas and oil. In shales, both mineral and organic matter usually contributes to the total porosity. Each of the existing porosimetry methods covers only a limited range of pore sizes, and the characterization of samples with wide pore size distribution generally requires application of several characterization methods (Fig. 1). The most common techniques that are used are helium porosimetry, low pressure nitrogen (N_2) and carbon dioxide (CO_2) adsorption, as well as mercury intrusion porosimetry (MIP). Several recent studies have used these techniques to understand pore size distribution in shales.[1-4] Small angle and ultra small angle neutron scattering (SANS/USANS) techniques have also been employed recently to study the structure of coals[5-6] and shales[2,3,7,8].

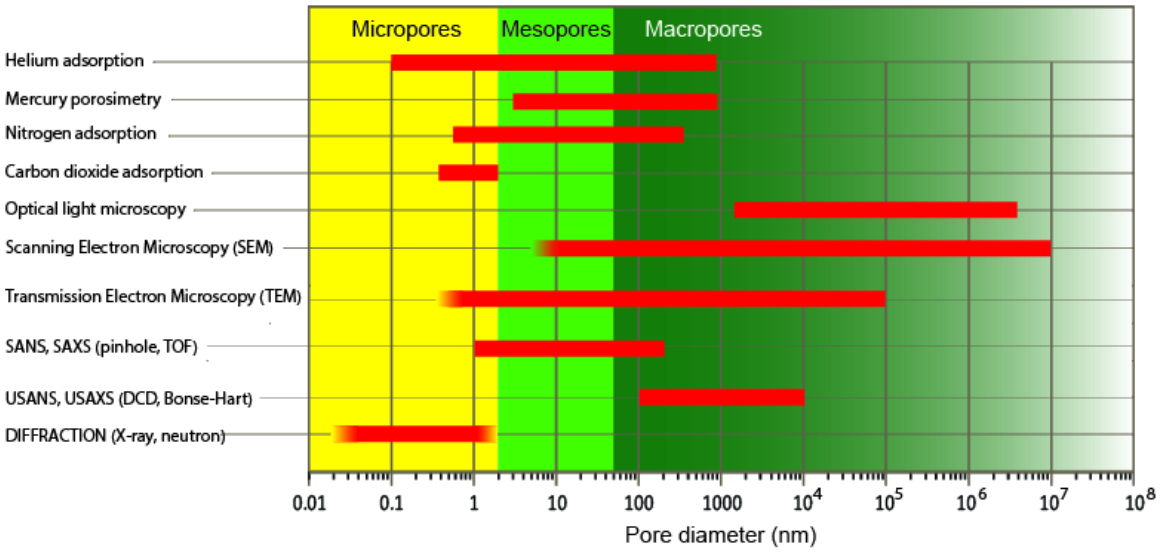

Figure 1. Comparison of the ranges of pore sizes that can be probed using various types of gas adsorption methods, optical microscopy, electron microscopy, neutron and X-ray scattering (partially adapted from Radlinski et al.[5]).

When comparing the sample porosity and pore size distribution determined using different techniques, it is important to remember that each of the techniques is based on different principles, and therefore some differences in the results may be expected. For example, in our recent paper[4] we directly compared porosity and pore size distribution data from gas adsorption and MIP techniques. As a rule, MIP provides information about the specific pore throat sizes that allow access to pore volumes. Pore throat size is an important parameter because it correlates with rock permeability and porosity[9-10]. There are several reasons to expect method-specific differences in pore size distribution and pore volume data from gas adsorption and MIP techniques when studying shales. Due to the small size of He and CO_2 gas molecules, they can access small nano-size pores and hence are ideal for probing microporosity. In contrast, mercury cannot penetrate micropores easily, and the necessity of using very high injection pressures (~380 MPa)

may cause artifacts due to distortion of the matrix structure, opening initially closed pores, and deforming the porous matrix.[11,12] In addition, MIP measures the size of pore throats, but not the actual pore body.

Our comparative study demonstrated that despite differences between the gas sorption and MIP techniques the measured pore volume and pore size distribution often qualitatively agree with each other.[4] This further suggests that these techniques are valuable and complementary for the structural characterization of shales, especially because each technique provides unique and specific information: MIP evaluates the size of pore throats, whereas gas adsorption assesses the distribution of pore body sizes.

Early small angle neutron scattering studies of coal and shale did not consider the small and relatively flat scattering background usually observed at the large Q-values. This approach was caused by intrinsic complexity involved in decoupling the incoherent background and scattering contribution from small micropores.[7,8,13,14] In general, to simplify the analysis of SANS data, the Q-independent scattering intensity at large-Q was subtracted from experimental scattering profile. Such a procedure is fully justified if population of micropores is not significant.

In the present work we demonstrate that neglecting the large-Q scattering part of SANS data may cause a significant underestimation of porosity by as much as an order of magnitude. A method has been developed to extract quantitative information of size distribution of nanopores from the large-Q scattering intensity.

The present study focuses on the investigation of pore morphology of the same set of New Albany Shale (Devonian/Mississippian) samples that were previously[4] analyzed using the gas adsorption and MIP techniques. The main objectives are (a) to compare

porosity obtained by SANS/USANS techniques with that determined by gas adsorption and MIP; (b) to analyse microporosity values extracted from SANS and USANS data, and (c) to discuss variation of porosity with increased maturity in shale detected by SANS/USANS.

2. Experimental

2.1 Samples

The New Albany Shale samples were collected from the core material archived at the Indiana Geological Survey and the Illinois State Geological Survey. The sampling sites were carefully selected to cover a range of maturities from immature to post mature. The mineral and chemical compositions as well as various properties of the pore space in aliquots of these samples were recently analysed using organic petrology, X-ray diffraction, CO_2 and N_2 low-pressure adsorption, and the mercury intrusion porosimetry.[4] Chemical composition of shale specimens is listed in Table 1.

The classification of pore sizes used in this paper follows the classification system of the International Union of Pure and Applied Chemistry (IUPAC).[15] According to IUPAC classification, pores with size greater than 50 nm are defined as macropores, whereas pores having size in the range 2–50 nm are called mesopores. The pores with size less than 2 nm are defined as micropores. Occasionally we use the name “nano-size pores” to indicate small mesopores and all micropores. It is to be noted that CO_2 was used to characterize micropores (<2 nm in diameter) as these pores are more accessible to CO_2 than to N_2.[4]

2.2 SANS and USANS Experiments

SANS and USANS experiment has been carried out on powder samples with grain size ~0.5 mm. The size of the grains is optimized in such a way that the scattering measurements provide the average information for all orientation of the grains and the scattering contribution from the grains as well as voids between the grains is negligible in the both SANS and USANS regime. The samples were put in Aluminum cell of 1.0 mm internal thickness. The effective thickness for the sample is ~ 0.5 mm, which helps in minimizing multiple scattering. SANS experiments were conducted using the General-Purpose SANS instrument[16] at Oak Ridge National Laboratory (ORNL). The sample detector distances (18.5, 6.0, and 0.25 m) were chosen to cover a wide range of scattering vectors Q of $0.001 < Q < 1.0$ Å^{-1}, where $Q = 4\pi\lambda^{-1}\sin(\theta)$ and 2θ is the scattering angle. The neutron wavelength λ was set to 4.75 Å for 0.25 and 6.0 m sample to detector distance. The neutron wavelength λ was set to 12.6 Å for 18.5 m sample to detector distance. The wavelength spread $\Delta\lambda/\lambda$ was 0.13. Scattered neutrons were detected using a 1×1 m^2 helium-filled two-dimensional (2D) position-sensitive detector with 192×192 pixels. The raw 2D data were corrected for the detector pixel sensitivity, empty Al cell scattering and dark current, and azimuthally averaged to produce a one-dimensional (1D) profile I(Q). USANS measurements were carried out at NIST, using the BT-5 perfect crystal SANS instrument (λ = 2.4 Å).[17] The Q range for USANS measurement was 4 x 10^{-5} Å^{-1} to 0.003 Å^{-1}. The wavelength spread $\Delta\lambda/\lambda$ was 0.06. The slit-smeared USANS data were converted into the pinhole geometry using Lake's method[18].

The Bragg law ($\lambda = 2r\sin\theta$, where for disordered systems r is the characteristic length scale of the structural inhomogeneities, e.g. linear pore size in a coal or shale

matrix), provides an approximate relationship between the scattering vector Q and r: $r \approx 2\pi/Q$. Detailed simulations show that for coal-like polydisperse porous media a more appropriate relationship is $r \approx \pi/Q$ (used in this work) or $r \approx 2.5/Q$.[19] Application of the GP-SANS and BT-5 instruments in a tandem allowed for a broad range of pore sizes, from approximately 4 Å to 40000 Å (0.0004 μm − 4 μm), to be probed by neutrons.

3. Results and Discussions

3.1 Estimation of Scattering Length Density

The purpose of this section is to calculate scattering length density for five New Albany Shale samples (472-1, MM4, NA2, IL-5 and IL-1). Table 1 lists the proportion of mineral components and the organic matter (TOC – Total Organic Carbon) in the shale samples, expressed in weight %. These numbers were converted to volume % using the matrix density for each component, also listed in Table 1.

Table 1. Volume proportion of minerals present in shale samples and volume-average matrix density calculated for five shales. [4] The grain density of the specimens was measured using Helium pycnometry.[4]

	dens (g/cm^3)	**472-1 (wt%)**	**472-1 (vol%)**	**MM4 (wt%)**	**MM4 (vol%)**	**NA2 (wt%)**	**NA2 (vol%)**	**IL-5 (wt%)**	**IL-5 (vol%)**	**IL-1 (wt%)**	**IL-1 (vol%)**
Quartz	2.65	20	20.48	35	30.84	36	34.53	32	31.31	26	25.42
Carbonates	2.80	51	49.42	0	0	1	0.91	26	24.08	10	9.25
Albite	2.61	8	8.32	9	8.05	13	12.66	6	5.96	29	28.8
Orthoclase	2.6	2	2.09	0	0	1	0.98	4	3.99	18	17.94
Pyrite	5.0	2	1.09	1	0.47	3	1.53	2	1.04	9	4.66
Clays	2.63	16	16.51	42	37.29	41	39.61	26	25.64	2	1.97
TOC	1.3	1	2.09	13	23.35	5	9.78	4	7.98	6	11.96
Total		100	100	100	100	100	100	100	100	100	100
Grain density g/cm^3			2.74		2.30		2.56		2.58		2.58

Neutron scattering length density was calculated for every component mineral using the formula [14]: $\rho_n = \frac{N_A d}{M} \sum_j p_j \left(\sum_i s_i b_i\right)_j$, where N_A=6.022 x 10^{23} is the Avogadro's number, d is density, s_i is the proportion by number of nucleus i in the compound j, p_j is the proportion of by molecular number of the compound j in the mixture and b_i is the coherent scattering amplitude for the nucleus i.

Results are presented in Table 2. As the exact composition and density for the organic matter dispersed in shales is not known, we used an estimated[20] value of SLD, corresponding to a low-ash coal (with maturity VR=0.67%, similar to organic matter in shale NA2): density =1.3 g/cm^3, SLD=2.5x10^{10} cm^{-2}.

Table 2. Numerical values used in calculations of the scattering length density for shale component minerals.

Mineral name	**Chemical formula**	**Matrix density d (g/cm^3)**	**Molecular weight M (g/mole)**	**Molecular scattering amplitude $\Sigma s_i b_i$ ($x10^{-12}$ cm)**	**SLD $=(N_A d/M)\ \Sigma s_i b_i$ ($x10^{10} cm^{-2}$)**
Quartz	SiO_2	2.65	60.085	1.5755	4.18
Carbonates	$CaCO_3$	2.80	100.0872	2.2309	3.76
Albite	$NaAlSi_3O_8$	2.61	262.2237	6.595	3.95
Orthoclase	$KAlSi_3O_8$	2.6	278.332	6.603	3.71
Pyrite	FeS_2	5.0	119.977	1.5234	3.62
Clays	$Al_2Si_2O_5(OH)_4$	2.63	263.161	5.2467	3.16
TOC	Coal analog	1.3			2.50

Finally, the SLD value was calculated for each shale as a volume-average over all component minerals according to the formula: $SLD\ (Shale) = \sum_i^n vol\%(i)SLD(i)/100$, where index i indicates a mineral component (including TOC) and n is the total number of components (including organic matter). The results are listed in Table 3.

3.2 Interpretation of SANS/USANS Results

Fig. 2 shows the plot of combined SANS and USANS absolute scattering cross section I(Q) in the units of cm^{-1} versus the scattering vector Q, acquired for five samples of New Albany Shale.

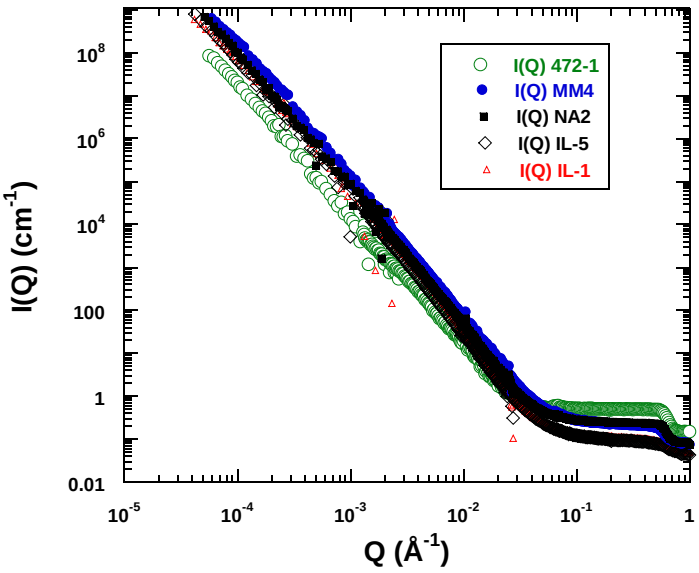

Figure 2. Combined SANS and USANS absolute scattering cross section I(Q) versus the scattering vector Q acquired for five samples of New Albany Shale.

The large-Q end of the scattering curve has been magnified and shown in Fig. 3. It is to be noted from Figs. 2 and 3 that reliable data extend up to Q≈0.5 $Å^{-1}$ only, due to the limited acceptance angle of sample holders used in this work. The scattering intensity at Q=0.5 $Å^{-1}$, called "flat" background, is indicated for each sample and depicted in Table 3. The background for shales 472-1 and NA2 is much larger than that typically observed for coal[13, 20] and is about an order of magnitude higher than the scattering background measured from most shales[2]. We note that the high background for MM4 shale may be caused by the large content of organic matter (23.4 vol%, Table 1).

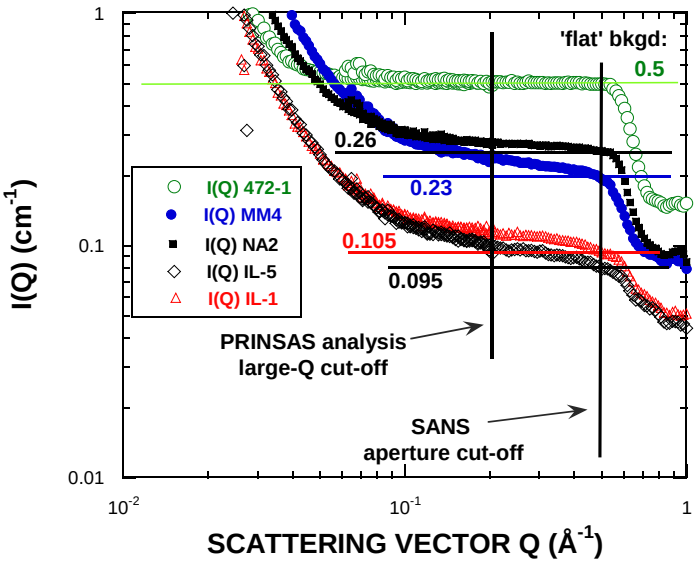

Figure 3. Large-Q SANS scattering measured from five studied samples of New Albany Shale. SANS aperture and PDSP model cutoffs and the flat background for each specimen are also indicated.

Table 3 Parameters used in the analysis of the five New Albany Shale samples. Helium grain density and bulk density were reported elsewhere [4]. Hydrogen content and incoherent background estimated for different shale samples from Fig. 4 is also shown.

	SLD (x 10^{10} cm^{-2})	**Flat BKG (cm^{-1})**	**He grain density* (g/cm^3)**	**Bulk density* (g/cm^3)**	**Depth (m)**	**TOC (wt%)**	**Ro (%)**	**H content (wt %)**	**Inc BKG (cm^{-1})**
472-1	3.74	0.5	2.74	2.49	61	1.2	0.35	0.5	0.027
MM4	3.39	0.23	2.3	2.21	764	13	0.55	3.0	0.16
NA2	3.57	0.26	2.56	2.43	853	5.3	0.65	1.4	0.074
IL-5	3.65	0.095	2.58	2.55	1607	4.3	1.15	0.6	0.032
IL-1	3.75	0.105	2.58	2.49	76	6.3	1.41	0.5	0.027

Two possible sources of the large-Q background are: (1) a Q-independent scattering background caused by the incoherent scattering of hydrogen atoms bound in the organic matter and sorbed water present in the rock, and (2) scattering from microscopic inhomogeneities (e.g. pores) present in the rock matrix. The hydrogen content has been estimated[4] based on the weight percent of organic matter and is listed in Table 3. Recently, Radlinski and Radlinska[20] demonstrated a correlation between hydrogen content and incoherent background, as shown in Fig. 4.

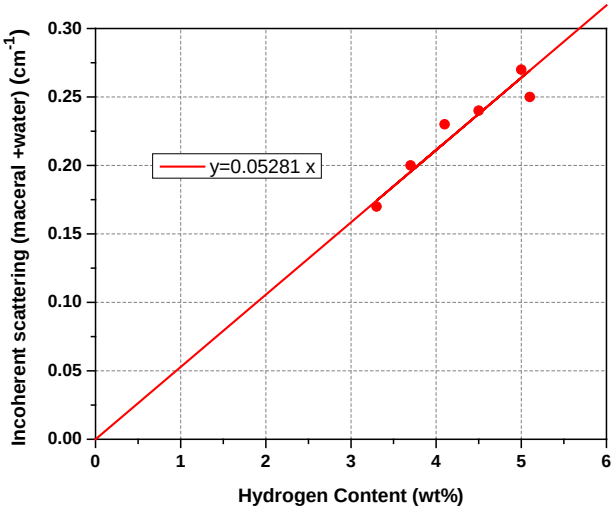

Figure 4. Correlation between the atomic hydrogen content and incoherent background used for estimation of incoherent background in New Albany Shale samples [20].

As may be seen in Table 3, the estimated incoherent background due to hydrogen content in the shale specimens is significantly less than the measured flat background, except for MM4 sample. This confirms that the measured high-Q background is not caused predominantly by the incoherent background. The origin of the anomalously large

flat background from the scattering data of the shale specimens will discussed in detail in the following section.

The neutron scattering data were analysed using the Polydisperse Spheres (PDSP) model[5], as implemented in PRINSAS software[21]. The PDSP model assumes that the pores are three-dimensional (spherical shape is used in the PRINSAS algorithm) and may have an arbitrary size distribution. Using the calculated value of the rock matrix scattering length density (SLD), the software fits the experimental scattering curve by adjusting the pore size distribution expressed as a histogram. Total porosity and other parameters characterizing the pore space are computed from that distribution.

First, the PDSP model was fitted to as-measured SANS/USANS I(Q) curves the Q-values less than 0.5 $Å^{-1}$, using the shale SLD and grain density values listed in Table 3. The quality of fit was generally very good, with the exception of the large-Q tail. As the first check of the validity of the PDSP model, the total porosity values generated by PRINSAS were compared with the known He porosity values (see Table 4). It transpired that the discrepancy between the two methods was over an order of magnitude, thus indicating that there is a significant scattering intensity component which is not well represented by the PDSP model. Thus, including in the PDSP model the flat scattering region up to 0.5 $Å^{-1}$ is not a physically viable option.

As the next step, the estimated flat background (see values listed in Table 3) has been subtracted from experimental data. It transpired that reliable (reasonably noise-free) data were then limited to Q-values smaller than about $Q_{max} \approx 0.2$ $Å^{-1}$ (Fig. 5). The scattering intensity approximately followed a power law over the Q-range used, which is indicative of approximately fractal distribution of the pore sizes. This implies that the flat

region of scattering profiles from 0.2 $Å^{-1}$ to 0.5 $Å^{-1}$ could not be represented by the PDSP model (*i.e.* the fractal model). In terms of real space that Q range transforms into linear size range from 5 Å to 12.5 Å. Thus, nano-size pores of radius within the range from 5 Å to 12.5 Å could not be represented by the fractal model.

The large-Q limit (Q=0.2 $Å^{-1}$) for fractal-like scattering used in revised PRINSAS analysis is also highlighted in Fig. 3. The PDSP model analysis was repeated using background- subtracted SANS data. The quality of fit was excellent (for examples see Fig. 6).

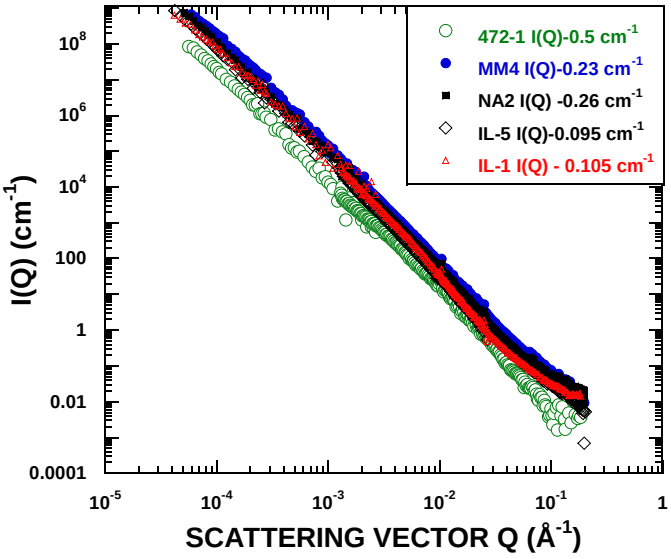

Figure 5. Combined SANS and USANS absolute scattering cross section (I(Q)) versus the scattering vector (Q) used for the PDSP model analysis for five samples of New Albany Shale. Compared to raw data the "flat" background has been subtracted, outlying data points removed, and the Q-range limited to the Q<0.2 $Å^{-1}$ region.

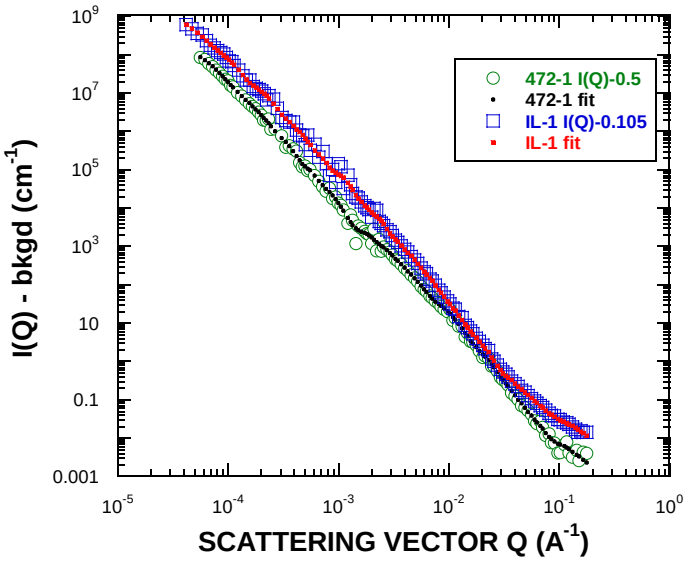

Figure 6. Illustration of the PDSP model fit for two of the New Albany Shale samples. Quality of fit for other samples is similar.

Table 4. Comparison of porosity values obtained using various methods for the five New Albany Shale samples. He Porosity and Hg intrusion porosity was calculated from the difference between grain density and bulk density measured by He pycnometry and Hg intrusion porosimetery, respectively.[4] Average value of fractal dimension (D_s) calculated for $Q<0.2Å^{-1}$ with the flat background scattering subtracted.

Samples	He Porosity (%)	Hg intrusion Porosity (%)	PDSP porosity $Q<0.5Å^{-1}$ (%)	PDSP fractal porosity $Q<0.2Å^{-1}$ (%)	Average fractal dimension D_s
472-1	9.1	5.6	82.8	0.47	2.6
MM4	4.1	2.7	55.7	4.4	2.8
NA2	5.1	4.1	55.7	2.64	2.8
IL-5	1.5	0.8	20.4	1.66	2.8
IL-1	3.5	1.4	21.8	1.79	2.8

Porosities obtained by fitting the PDSP model to the background-subtracted SANS data including Q-values up to 0.2 $Å^{-1}$ agree better with the He porosities (Table 4). The PDSP model porosity for MM4, IL-5 specimens is very close to their respective He porosity. The least mature sample 472-1 had particularly small PDSP porosity compared to He porosity. Similarly, estimated porosity for NA-2 and IL-1 specimens shows significant difference (by a factor of two) from He porosity.

It is important to mention at this juncture that CO_2 adsorption measurements on these shales indicate presence of micropores of size less than 2 nm.[4] However, the PDSP model analysis does not include pores of size less than 2.5 nm. It has also been concluded

from CO_2 adsorption data that the contribution to the porosity due to micropores is quite large for samples 472-1, NA-2 and IL-1 compared to samples MM4 and IL-5. Therefore, it follows that the porosity calculated using the PDSP model for the former samples may be significantly underestimated due to the exclusion of large fraction of the micropores. We also note that the scattering profile at large Q-values (which is dominated by contribution from micropores) does not follow a straight line on the double logarithmic scale (Fig. 3). Hence, the size distribution of the micropores excluded from the PDSP model should not be considered fractal.

Detailed results of structural analysis for all shales (obtained using the PDSP model) are presented in Supplementary Information. Total volume of mesopores and macropores estimated by different techniques are compared in Fig. 7 and Fig. 8.

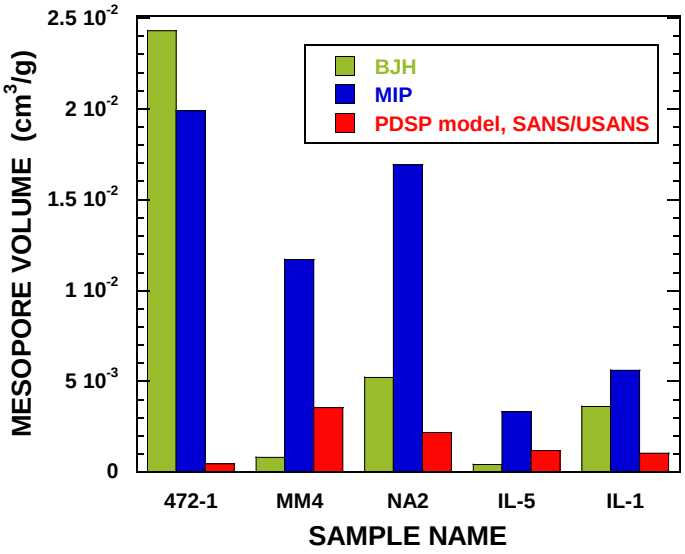

Figure 7. Mesopore volumes (pore radius 1-25 nm) for the five samples of New Albany Shale, measured using three different methods: (1) N_2 and CO_2 adsorption, (2) mercury intrusion porosimetry and (3) PDSP analysis of SANS/USANS.

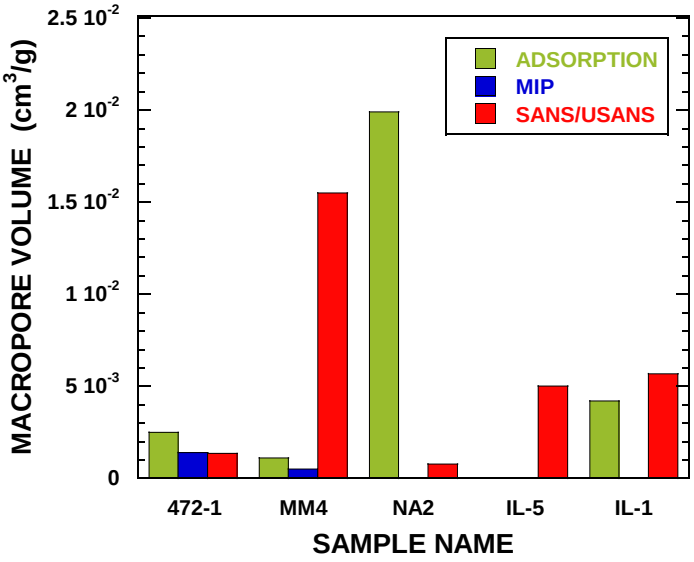

Figure 8. Macropore volumes (pore radius larger than 25 nm) for the five samples of New Albany Shale, measured using three different methods: (1) N_2 and CO_2 adsorption, (2) mercury intrusion porosimetry and (3) PDSP analysis of SANS/USANS.

Porosity in the mesopore region estimated by SANS/USANS is low compared to that measured by N_2 adsorption and MIP method (Fig. 7). This is expected since the PDSP porosity was estimated using SANS data truncated at the large-Q end. Therefore, a significant population of mesopores of diameter between 2 nm to 2.5 nm was not included in the PDSP fits. The magnitude of the underestimate depends on the actual number density of mesopores smaller than the cut-off size. Since the combined micro- and mesoporosity is largest for shale 472-1, this sample also exhibits the largest discrepancy between the PDSP and sorption results. Similar reasoning can be used to interpret discrepancies observed for other samples.

In addition to the large-Q SANS truncation effects, observed differences in porosities measured by gas adsorption and SANS/USANS techniques may be partly

attributed to (1) existence of micropores not well described by the PDSP model and, importantly, (2) N_2 and CO_2 fluid condensation in the smallest micropores.

Total pore volumes of macropores, estimated using various techniques, are shown in Fig. 8. Macropore volumes for shales 472-1 and IL-1 are in a generally good agreement with each other. However, the macropore volume estimated by SANS/USANS analysis for shale MM4 is large compared to MIP and adsorption data, which may be due to the presence of significant number of pores which are not accessible to the invading fluids. For the shale NA2 the macropore volume determined by adsorption is large compared to that estimated by SANS/USANS. This is a puzzling result, which could be possibly explained by different pore geometry assumed in the analysis of adsorption and scattering data.

3.3 Porosity Calculations using Porod Invariant

The model-independent Porod invariant method has been applied to estimate the porosity of shale samples. For a two-phase system (rock matrix and the pore space), the porosity, ϕ, can be calculated from Porod Invariant, Q_{inv}:

$$Q_{inv} = \int_0^\infty Q^2 I(Q) dQ = 2\pi^2 (\Delta\rho)^2 \phi(1-\phi) \quad (1)$$

The value of the integral is sensitive to the precision with which the scattering intensity has been determined, which in turn is strongly affected by the choice of the large-Q scattering background. This is demonstrated in Table 5, which shows (1) a comparison of porosity calculated using the polydisperse sphere (PDSP) model and the Porod Invariant method (with the same large-Q background determined assuming a near-fractal scattering as illustrated in Fig. 3 and listed in Table 5) and (2) an empirical value of the

large-Q background estimated to match the independently measured helium porosity value for each sample.

Table 5 Porosity values estimated using Porod Invariant (PI) and PDSP model for the same large-Q background. He porosity compatible background is the background which is subtracted from the experimental scattering profile to achieve the He porosity in Porod Invariant method.

Sample	Near-fractal large-Q background (cm^{-1})	PDSP porosity (%)	PI porosity (%)	Helium porosity (%)	He porosity compatible large-Q bkgd (cm^{-1})
472-1	0.50	0.47	0.699	9.1	0.455
MM4	0.23	4.4	4.05	4.1	0.23
NA-2	0.26	2.64	3.22	5.1	0.25
IL-5	0.095	1.66	1.58	1.5	0.095
IL-1	0.105	1.79	1.92	3.5	0.090

It is evident from Table 5 that porosities estimated using the PDSP model and Porod Invariant method for the same background data are close to each other, as expected. An empirical value of the background which needs to be subtracted from experimental I(Q) to obtain the porosity of the sample equal to He porosity when the Porod Invariant method is used, has been calculated. Comparison of the large-Q background and the calculated empirical background values (columns 2 and 6, Table 5) and of the corresponding porosity values (columns 4 and 5, Table 5) well illustrates high sensitivity of the estimated porosity to the value of the large-Q background.

3.4 The Origin of Large-Q Background

The large-Q background values measured in this work cannot be attributed to the incoherent scattering on hydrogen nuclei bound in the organic component of the rock matrix. Fig. 9 illustrates that there is no positive correlation between the intensity of large-Q background and organic matter content (TOC) in the five shales, which proves the point. Such a conclusion is to be expected, since at the quantitative level, the incoherent scattering intensity for a low-ash coal of a similar density and chemical composition of the organic matter can be calculated as 1/20 of the hydrogen wt%: $I(incoh)[cm^{-1}] \approx 0.053(H[wt\%])$[19]. Using hydrogen content values listed in Table 3, the incoherent scattering can be shown to be small (but not insignificant) compared to the measured SANS background for each shale sample (Table 3).

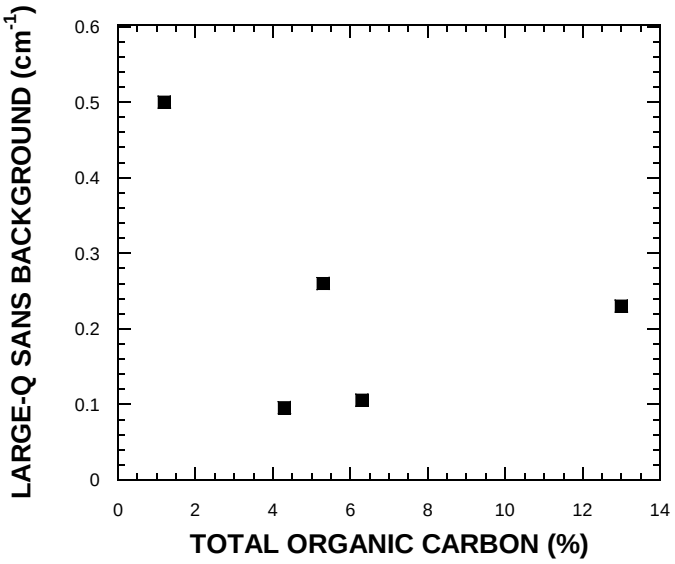

Figure 9. Cross-plot of scattering intensity at Q=0.5Å^{-1} (large-Q background) and total organic matter content (TOC in units of wt %) for five shales.

Looking at the porosity data listed in Table 4, it appears that (within experimental error of roughly +/- 0.1%) the helium porosity usually matches or exceeds the PDSP model (SANS/USANS) porosity. Assuming that helium gas molecules can penetrate all pores accounted for by SANS and USANS (i.e., pores larger than about 12.5 Å in body radius), one can assign the difference between the He porosity and PDSP porosity (excess porosity, or non-fractal porosity, Φ_{ex}) to very small nanopores (body radius < 12.5 Å). Scattering from these nanopores contributes to the large-Q background, in addition to scattering from closed nanopores and the incoherent background.

In order to test the above hypothesis, the excess porosity Φ_{ex} is plotted as a function of the large-Q scattering background (Fig. 10). There is some scattering in the data, but the fitted line suggests the following approximate relationship: Φ_{ex} = -2.2 + 20*bkgd, where Φ_{ex} is expressed in % and the background, bkgd, in cm^{-1}. We can understand the above observation as follows. There are some closed (inaccessible to helium fluid) nanopores, which (together with the incoherent scattering) give rise to a scattering background component of 0.11 $cm^{-1.}$ Any scattering above this level is caused by He-accesssible (open) pores. The large-Q SANS results available to us (almost flat background only) provides no information about the geometry of these pores.

Going one step farther, one can estimate the incoherent scattering intensity using the approach outlined in Fig. 4 and Table 3. The incoherent free background, if_bkgd, can be estimated by subtracting the incoherent contribution from the large-Q background. The excess microporosity Φ_{ex} has been shown in Fig. 11 as a function of incoherent free background. The linear fit is markedly improved compared to Fig. 10, and

the approximate relationship between the excess nano-porosity and the incoherent-free background is: $\Phi_{ex} = -1.2 + 20.5 \times if\_bkgd$

where Φ_{ex} is expressed in % and the incoherent-free background, if_bkgd, in cm^{-1}. The scattering component of He-inaccessible pores only (without the incoherent component), for which $\Phi_{ex} = 0$, can be estimated as 0.059 cm^{-1}. Any scattering above that is caused by accessible non-fractal nanopores. The described procedure provides a method of estimating the non-fractal nanoporosity value (called microporosity in the organic geochemistry literature) from the measurements of large-Q background, at least for the New Albany Shale rocks.

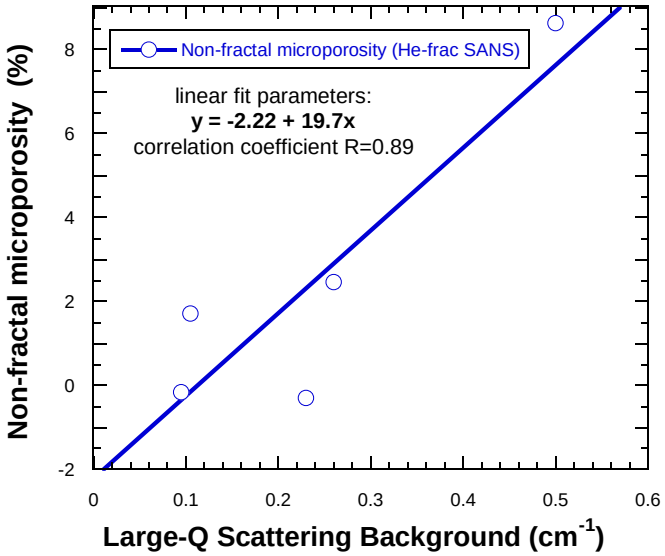

Figure 10. Cross-plot of the excess total porosity Φ_{ex} versus scattering intensity at Q=0.5$Å^{-1}$ (large-Q scattering background). Excess porosity is dominated by micropores of linear body size smaller than 12.5 Å and unknown shape and origin. Fitted line suggests the following approximate relationship: $\Phi_{ex} = -2.2 + 20 \times \text{bkgd}$, where Φ_{ex} is expressed in % and the "flat"background, bkgd, in cm^{-1}.

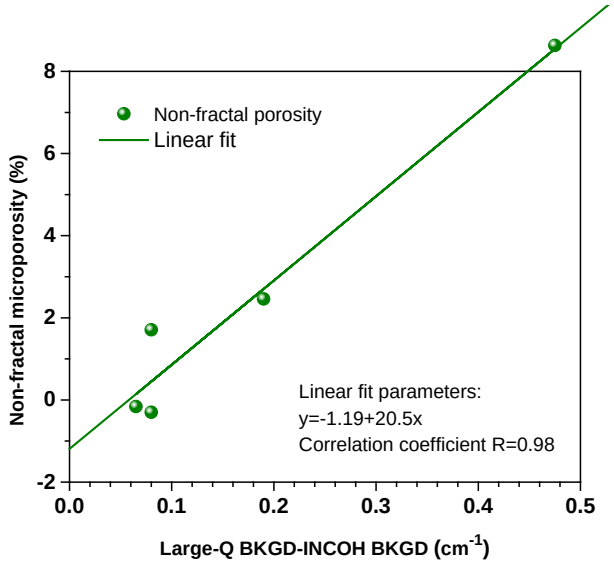

Figure 11. Cross-plot of the excess total porosity, Φ_{ex} versus scattering intensity at Q=0.5Å^{-1} with incoherent background subtracted. Fitted line suggests the approximate relationship:$\Phi_{ex} = -1.2 + 20.5 \times \text{if\_bkgd}$, where Φ_{ex} is expressed in % and the incoherent-free background, if_bkgd, in cm^{-1}.

3.5 Trends in Shale Porosity as a Function of Maturity

Finally, the total porosity and microporosity of shale specimens was analyzed as a function of sample maturity. Figures 12a and 12b illustrate the apparent correlation between (a) total porosity and (b) PDSP porosity and the incoherent-free fraction of the large-Q background versus thermal maturity of the organic matter (expressed in terms of vitrinite reflectance).

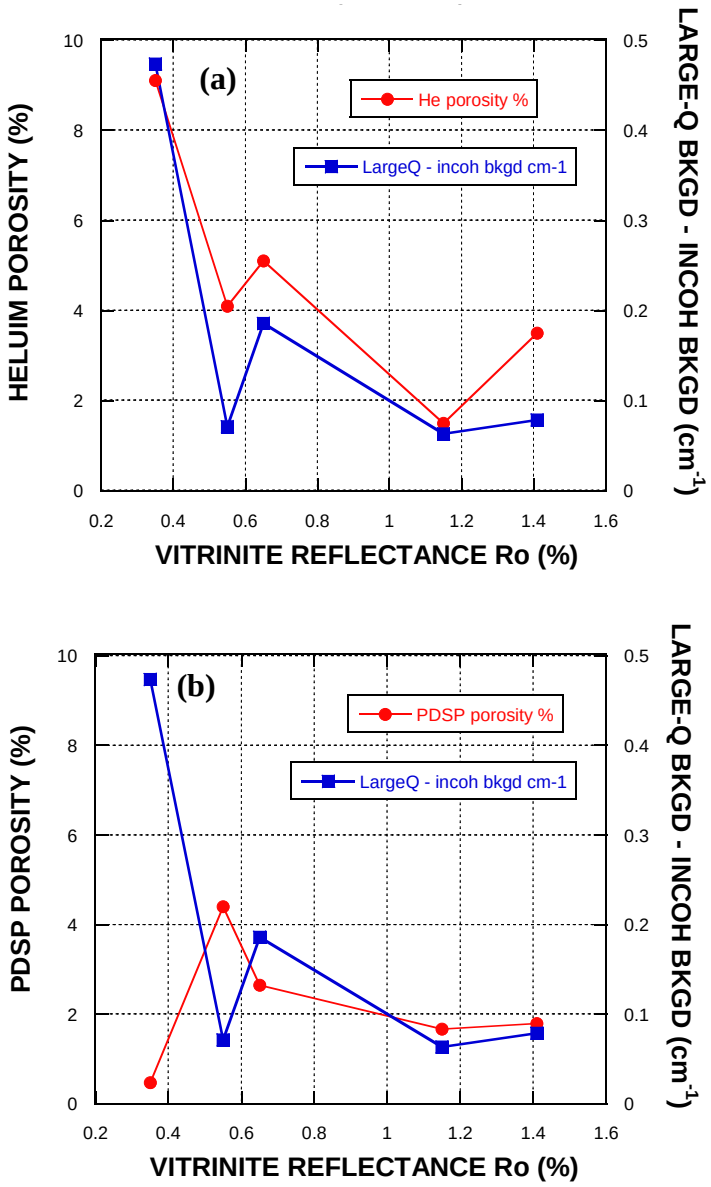

Figure 12. Incoherent free background and (a) Total porosity (b) PDSP porosity as a function of shale maturity.

The porosity decreases generally with increasing maturity of the organic matter. This is expected, as thermal maturity is a proxy for the depth of burial (achieved at some time between the deposition and the present time), and the larger depth of burial leads to more pronounced compaction of the rock matrix. This general trend can be, however,

modified by the processes related to the organic matter transformation and hydrocarbon generation, as was suggested for this set of samples in the previous study[4]. The fact that the incoherent-free large-Q background decreases in step with total helium porosity strongly suggests that the background is most likely caused by the (compaction-affected) nano-size porosity rather than the short-range inhomogeneity of the chemical composition of the rock matrix. Correlation between the microporosity and the large-Q background is not that clear-cut when the PDSP porosity rather than helium porosity is used (Fig. 12b). However, this may simply be a consequence of the approximate procedure by which the large-Q background has been determined (the near-fractality assumed for the I(Q) function), which is subject to the particularly large uncertainty for the largest measured background (for sample 472-1, Ro=0.35%, in this case).

3.6 Estimates of the size and number density of nanopores contributing to the large-Q background

In this section we estimate the range of size as well as the number density of micropores (both accessible and inaccessible to He fluid) which contribute to the large-Q scattering background. We assume that the nano-size pores are three-dimensional, dilute and isotropic, and are roughly monodisperse in size for each rock sample.

According to the Guinier law, for $QR_g<<1$ scattering from such a system is given by:

$$I(Q) = n(\Delta\rho V)^2 exp\left[-\frac{Q^2 {R_g}^2}{3}\right] \approx n(\Delta\rho V)^2\left[1 - \frac{Q^2 {R_g}^2}{3} + \cdots\right] \quad (2)$$

where n is the number density of the scatterers of volume V (in units of cm^{-3}), Δρ is the scattering contrast and R_g is the radius of gyration of the scatterers. We assume that the nearly flat scattering intensity, I_0, observed for all samples at the large Q-values ($Q \geq 0.4$ $Å^{-1}$, Fig. 3) corresponds to the sum of the incoherent scattering, I_{incoh}, and the saturation value of the Guinier region for the nano-size scatterers, $I(Q_{sat})$. The notation $I(Q_{sat})$ indicates nanopore scattering intensity at some Q-value such that (1) $Q << 1/r_{ns}$ and (2) the contribution of scattering from the larger pores (e.g. fractal scattering) is negligible, where r_{ns} is radius of the micropore.

According to eq. 2, the saturation value for the nano-size pore scattering is:

$$I(Q_{sat}) = n(\Delta\rho V)^2 \quad (3)$$

Since the numerical values of both $I(Q_{sat})$ ~ [(large-Q bkgd) - I_{incoh}] and Δρ are known (Table 3), eq.3 describes a relationship between the estimated scatterer radius, r, (here calculated from $V=4/3\pi r^3$) and the number of scatterers per unit volume, n, for each sample. As the fraction of sample volume occupied by scatterers (i.e. sample porosity, Φ) is nV, it is convenient to rearrange eq.3 into the form:

$$I(Q_{sat}) = nV(\Delta\rho)^2 \frac{4}{3}\pi r^3 = \Phi(\Delta\rho)^2 \frac{4}{3}\pi r^3 \quad (4)$$

Equation 4 can be used to create a plot of porosity versus scatterer radius and narrow down the range of possible (monodisperse) scatterer sizes (Fig. 13).

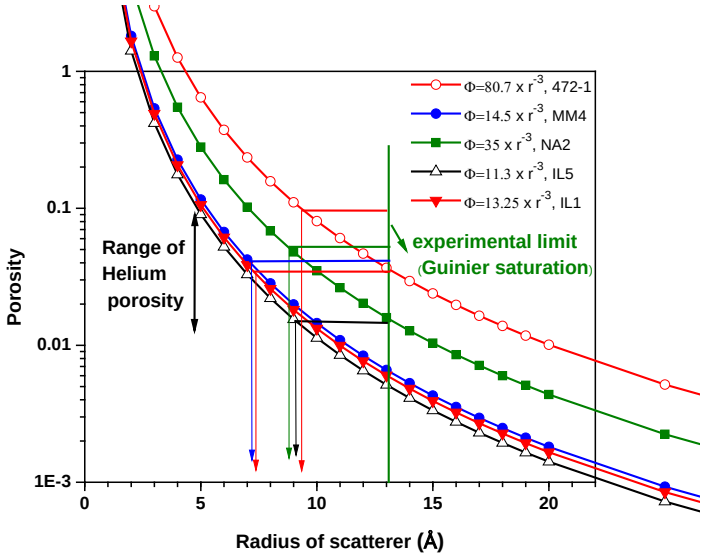

Figure 13. Graphic representation of the theoretically allowed porosity values versus the monodisperse scatterer size. For detailed description see text.

In Fig. 13, five different symbols are used to show the relationship between the scatterer size and the number of scatterers (expressed as the porosity, $\Phi=nV$), which is consistent with the incoherent-free scattering intensity, $I(Q_{sat})$, measured for the five samples of New Albany Shale. The colour-coded horizontal lines indicate the helium porosity value for each sample. The intersection of such line with the curve interpolated between symbols corresponding to the same sample determines the minimum radius of hypothetical monodisperse nanopores, as indicated with colour-coded vertical arrows. In reality, the nanopores account for only a (unknown) fraction of the total helium porosity and, therefore, the scatterer radii must be larger than their minimum values indicated in Fig. 13. On the other hand, the nano scatterer radius cannot be larger than about $2\pi/0.5 \approx 12.5$ Å, since the I(Q) curves presented in Fig. 3 seem to be fully saturated for every

sample at the experimental upper limit of the Q-range, equal to Q=0.5 $Å^{-1}$. The experimental Guinier saturation limit is indicated with a vertical green line in Fig. 13. It follows from Fig. 13 that the large-Q SANS data are consistent with the existence of nanopores with linear sizes (radii) within the range 7-13 Å for samples MM4 and IL-1, and 9-13 Å for samples 472-1, NA2 and IL-5. SANS detection of scatterers of such sizes is in principle possible, however it requires access to scattering data at values of Q much larger than those accessible in our experiments.

Since the fraction of total porosity contained in micropores is not precisely known one can only gain a limited insight into the number density, n, of nanopores. Based on the relationship illustrated in Fig. 13, Table 6 lists estimates of the value of n for two scenarios: (1) total helium porosity is contained in monodisperse nanopores of radius r and (2) all nanopores are monodisperse and have the same radius for every shale sample (12 Å), which is close to the maximum possible radius consistent with our data. This estimate is done for illustrative purposes only.

It follows that the number density of nanopores in the New Albany Shale samples may vary from about $1x10^{18}$ cm^{-3} to about $3x10^{19}$ cm^{-3}, assuming that pores are three-dimensional and roughly monodisperse (Table 6). Fig. 14 illustrates the correlation between the nanopore number density and the thermal maturity of organic matter for the five samples according to the two scenarios.

Table 6 Nanoporosity and number density of nanopores calculated according to scenarios 1 and 2. Single nanopore volume for r = 12 Å is 7.24×10^{-21} cm^3. For details see text.

Sample	Helium porosity (= nV) (%)	Nanopore radius r (Å)	Single nanopore volume $4\pi r^3/3$ ($x10^{-21}$ cm^3)	**Scenario 1** Nanopore number density n ($x10^{19}$ cm^{-3})	Porosity for r=12 Å (from Fig. 13) (%)	**Scenario 2** Nanopore number density n ($x10^{18}$ cm^{-3})
472-1	9.1	9.7	3.8	2.4	4.7	6.5
MM4	4.1	7.0	1.44	2.85	0.86	1.2
NA2	5.1	8.9	2.95	1.73	2.1	2.9
IL-5	1.5	9.2	3.26	0.46	0.66	0.91
IL-1	3.5	7.4	1.7	2.06	0.77	1.1

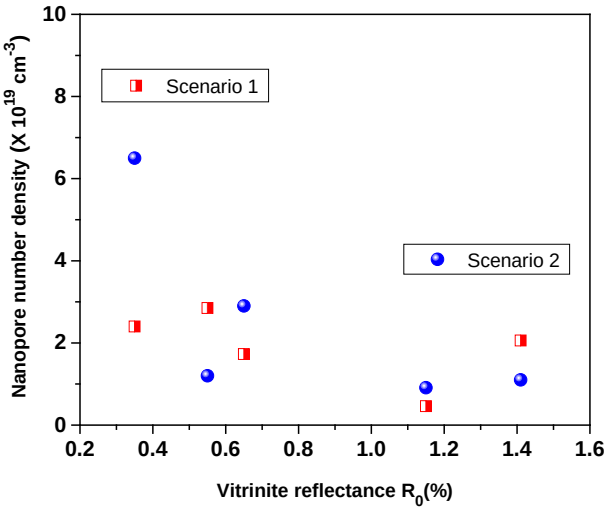

Figure 14. Number density of micropores calculated according to scenario 1 and scenario 2 plotted versus thermal maturity of organic matter, for five New Albany Shale samples.

Comparing these estimates with CO_2 adsorption data[4], which indicate elevated microporosity for shale 472-1, scenario 2 (nano-size pores are monodisperse and similar in size for every shale) appears to be more plausible than scenario 1.

Conclusions

SANS results indicate that pores in the New Albany Shale samples can be divided into fractal and non-fractal, depending on the pore size. Macropores (>50 nm) and the majority of mesopores (2-50 nm) are surface fractals and their structure is well represented by the PDSP model. In the mesopore region, the total porosity computed from SANS/USANS data significantly differs from that determined by gas adsorption and MIP technique, most likely because of the exclusion of significant population of mesopores due to truncation of neutron scattering data. Other factors, such as the possible condensation of invading fluid in nano-sized pores and assumption of specific pore geometry may also play a role. SANS results suggest that for the immature to post-mature shales, microporosity is highest in the least mature samples and decreases with shale maturity. At the same time, microporosity increases slightly for post-mature shale specimens. Scattering from non-fractal micropores (<2 nm) contributes significantly to the high-Q flat background. A newly developed method of SANS/USANS data analysis allows extracting qualitative information on the structure of micropores (such as the size range and number density) from that background. The method is general and may provide information on the morphology of nano-size pores in natural and engineered porous systems.

Supporting Information

Detailed results of PDSP modeling of the structure of five shale samples are presented in Supporting Information. The data include: variation of the internal specific surface area as a function of probe size (Fig. S1), pore body radius distribution (Fig. S2), incremental pore volume dV/dr (Fig. S3) and the cumulative pore volume (Fig. S4). All results were obtained using SANS/USANS data in the Q-range from $5x10^{-5}$ $Å^{-1}$ to 0.2 $Å^{-1}$.

Acknowledgments

The authors would like to acknowledge D.F.R. Mildner for his help during USANS experiments. The research at Oak Ridge National Laboratory's High Flux Isotope Reactor was sponsored by the Laboratory Directed Research and Development Program and the Scientific User Facilities Division, Office of Basic Energy Sciences, U.S. Department of Energy. This research was supported in part by the ORNL Postdoctoral Research Associates Program, administered jointly by the ORNL and the Oak Ridge Institute for Science and Education. This study was also partly supported by U.S. Department of Energy, Office of Science, Office of Basic Energy Sciences under Award Number Grant DE-SC0006978 (formerly DE-FG02-11ER16246). This work utilized facilities supported in part by the National Science Foundation under Agreement No. DMR-0454672. We acknowledge the support of the National Institute of Standards and Technology, U.S. Department of Commerce, in providing the neutron research facilities used in this work.

References

(1) Chalmers, G. R.; Bustin, R. M.; Power, I. M. *AAPG Bulletin* **2012**, 96, 1099–1119.

(2) Clarkson, C.R.; Freeman, M.; He, L.; Agamalian, M.; Melnichenko, Y.B.; Mastalerz, M.; Bustin, R.M.; Radlinski, A.P.; Blach, T.P. *Fuel* **2012**, 95, 371-385.

(3) Clarkson, C. R.; Solano, N.; Bustin, R. M.; Bustin, A. M. M.; Chalmers, G. R. L.; He, L.; Melnichenko, Y. B.; Radliński, A. P.; Blach, T. P. *Fuel*, **2013**, 103, 606-616.

(4) Mastalerz, M.; Schimmelman, A.; Drobniak, A.; Chen, Y. *AAPG Bulletin*, **2013**, 97, 1621-1643.

(5) Radlinski, A.P.; Mastalerz, M.; Hinde, A.L.; Hainbuchner, M.; Rauch, H.; Maron, M.; Lin, J.-S.; Fan, L.; Thiyagarajan, P. *International Journal of Coal Geology* **2004**, 59, 245-271

(6) Melnichenko, Y.B.; He, L.; Sakurovs, R.; Kholodenko, A.L.; Blach, T.; Mastalerz, M.; Radlinski, A.P.; Cheng, G., Mildner, D.F.R *Fuel* **2012**, 91, 200-208

(7) Mastalerz, M.; He, L.; Melnichenko; Y. B.; Rupp, J. A. *Energy & Fuels* **2012**, 26, 5109–5120

(8) Ruppert, L.F.; Sukurovs, R.; Blach, T.P.; He, L.; Melnichenko, Y.B.; Mildner, D.F.R.; Alcantar-Lopez, L. *Energy and Fuels* **2013**, 27, 772-779.

(9) Nelson, P. H.; Batzle, M. L. *Single-phase permeability, in J. Fanchi, ed.*, *Petroleum engineering handbook: Volume I: General engineering: Richardson,* Texas, Society of Petroleum Engineers 2006, 1 ,pp 687–726

(10) Nelson, P. H. *AAPG Bulletin* **2009**, 93, 329–340

(11) Bustin, R. M.; Bustin; A. M. M.; Cui, X.; Ross, D. J. K.; Murthy Pathi, V. S. *SPE Paper No 119892,* **2008** *presented at the SPE Shale Gas Production Conference, Society of Petroleum Engineers, Fort Worth, USA, 16-18 November, 2008*, doi: 10.2118/119892-MS

(12) Kuila, U.; M. Prasad *SPE Paper No 146869,* **2011** *presented at the SPE Annual Technical Conference and Exhibition, Denver, USA, 30 Oct – 2 Nov, 2011*, http://www.spe.org/atce/2011/pages/schedule/tech_program/documents/spe146869%201.pdf

(13) Jin, L.; Rother, G.; Cole, D. R.; Mildner, D. F.R.; Duffy, C. J.; Brantley, S. L. *American Mineralogist* **2011**, 96, 498–512.

(14) Radlinski, A.P. *"Small Angle Neutron Scattering & Rock Microstructure". In: Reviews in Mineralogy and Geochemistry, 63*: Neutron Scattering in Earth Sciences, 2006, Chapter 14, pp. 363-397 (H-R Wenk editor)

(15) Orr, C. *Surface area measurement, in I. M. Kolthoff, P. J. Elving, F. H. Stross, eds., Treatise on analytical chemistry: Part III: Analytical chemistry in industry,* New York, John Wiley and Sons **1977**, 4, pp 321–358.

(16) Wignall, G. D.; Littrell, K. C.; Heller, W. T.; Melnichenko, Y. B.; Bailey, K. C.; Lynn, G.W.; Myles, D. A.; Urban, V. S.; Selby, D. L. *J. Appl. Cryst.* **2012**, 45, 990-998.

(17) Barker, J. G.; Glinka, C. J.; Moyer, J. J.; Kim, M. H.; Drews, A. R.; Agamalian, M. *J. Appl. Crystallogr.* 2005, **38**, 1004−1011.

(18) Lake, J. A. Acta Cryst. **1967**, 23, 191-194.

(19) Radlinski, A. P.; Boreham, C. J.; Lindner, P.; Randl, O.; Wignall, G. D.; Hinde, A.; Hope, J. M. *Org. Geochem.* **2000**, 31, 1−14.

(20) Radlinski, A.P.; Radlinska, E.Z. *"The microstructure of pore space in coals of different rank: a small angle scattering and SEM study". In: Coalbed Methane: Scientific, Environmental and Economic Evaluation*, Kluwer Academic Publishers, Dodrecht 1999, pp 329-365 (M.Mastalerz, M. Glikson and S.D. Golding editors).

(21) Hinde, A.L. *J. Appl. Crystallogr.* **2004**, 37 1020-1024.